Journal of Energy Chemistry 51 (2020) 378–387

Contents lists available at ScienceDirect

Journal of Energy Chemistry

journal homepage: www.elsevier.com/locate/jechem

http://www.journals.elsevier.com/journal-of-energy-chemistry/

Confining sulfur in intact freestanding scaffold of yolk-shell nanofibers with high sulfur content for lithium-sulfur batteries

Xilai Zhang[a,b,1], Peng Zhang[a,b,c,1,*], Shijie Zhang[a,b,c], Yongshang Zhang[a,b,c], Ruohan Hou[a,b], Kangli Liu[a,b], Fujun Miao[a,b,c,*], Guosheng Shao[a,b,c,*]

[a] School of Materials Science and Engineering, Zhengzhou University, Zhengzhou 450001, Henan, China
[b] State Centre for International Cooperation on Designer Low-Carbon & Environmental Materials (CDLCEM), Zhengzhou University, Zhengzhou 450001, Henan, China
[c] Zhengzhou Materials Genome Institute, Xingyang 40100, Henan, China

ARTICLE INFO

Article history:
Received 16 February 2020
Revised 26 March 2020
Accepted 26 March 2020
Available online 24 April 2020

Keywords:
TiO_2
TiN
Electrospinning
Lithium-sulfur batteries
Carbon nanofibers
Yolk-shell structure

ABSTRACT

Nanostructure design holds great potential in fabricating sulfur electrodes that host a high sulfur loading and still attain high electrochemical utilization for the developing of high-energy-density lithium-sulfur (Li-S) batteries. In this contribution, we introduce the yolk-shell structure into a freestanding carbon nanofibers film and construct a complete hollow yolk-shell TiO_2/carbon nanofibers@void@TiN@carbon (TiO_2-CNFs@void@TiN@C) composite. With inherent double conductive network and strong adsorption capability for polysulfides, the TiO_2-CNFs@void@TiN@C composite can not only provide sufficient electrical contact for the insulating sulfur, but also effectively entrap polysulfides for prolonged cycle life. As a result, an excellent capacity retention ratio of 60.9% after 1000 cycles at 1 C as well as a high capacity of 688.5 mAh g^{-1} at 5 C rate is accomplished with the cells employing TiO_2-CNFs@void@TiN@C as a cathode substrate for sulfur. Moreover, the TiO_2-CNFs@void@TiN@C composite, with a high S mass loading of 9.5 mg cm^{-2}, delivers a superb areal capacity of 8.2 mAh cm^{-2}.

1. Introduction

Lithium-sulfur (Li-S) batteries have been considered as one of the most promising candidates for the next-generation energy storage technique due to its ultrahigh theoretical capacity (1675 mAh g^{-1}) and earth abundance [1–5]. However, the commercialization of Li-S batteries has been impeded by three main issues: (a) The low utilization of the active material caused by the poor conductivity of sulfur and its discharge product Li_2S or Li_2S_2; (b) the poor electrode structural stability arising from the large volumetric expansion (nearly 80%) during the charge-discharge process; (c) the irreversible capacity decay incurred from the shuttle effect of the intermediate lithium polysulfides (LiPSs) [5–8]. Accordingly, great efforts have been devoted to developing novel strategies to address the above issues. Among these attempts, employing the composites of carbonaceous materials and polar groups as sulfur hosts were widely reported [9–12]. For example, Wang's group reported a porous freestanding S/TiO_2-CNFs composite as a cathode [13]. Benefitting from the high conductivity of CNFs and the strong chemically adsorption to LiPSs of TiO_2, this freestanding cathode achieved an excellent rate performance. However, this one-dimensional structure can hardly achieve a high sulfur loading because its finite catalytic and adsorption effect cannot afford the excessive accumulated LiPSs [14–18].

Recently, the functionalized interlayers between the separator and cathode were widely used to confine the LiPSs and enhance the catalytic conversion efficiency of LiPSs [19–22]. For example, Ding's group synthesized an integrated multilayered S-CNTs/CoNCNFs/PVDF fibrous membrane by electrospinning and base-coating techniques [23]. Under the synergistic effects of each functional layer, this fibrous membrane showed a long-life cyclability even under high sulfur loading. Although the functionalized interlayers can provide targeted solutions to the problems in Li-S batteries(carbonaceous interlayers to improve conductivity and physically intercept the migrating LiPSs [24,25], polar functional interlayers to intercept the migrating LiPSs and enhance the catalytic conversion efficiency of LiPSs [21,26]), the increased volume

* Corresponding authors at: School of Materials Science and Engineering, Zhengzhou University, Zhengzhou 450001, Henan, China.
E-mail addresses: zhangp@zzu.edu.cn (P. Zhang), miaofj@zzu.edu.cn (F. Miao), gsshao@zzu.edu.cn (G. Shao).
[1] Both the authors contributed equally to this work.

https://doi.org/10.1016/j.jechem.2020.03.065

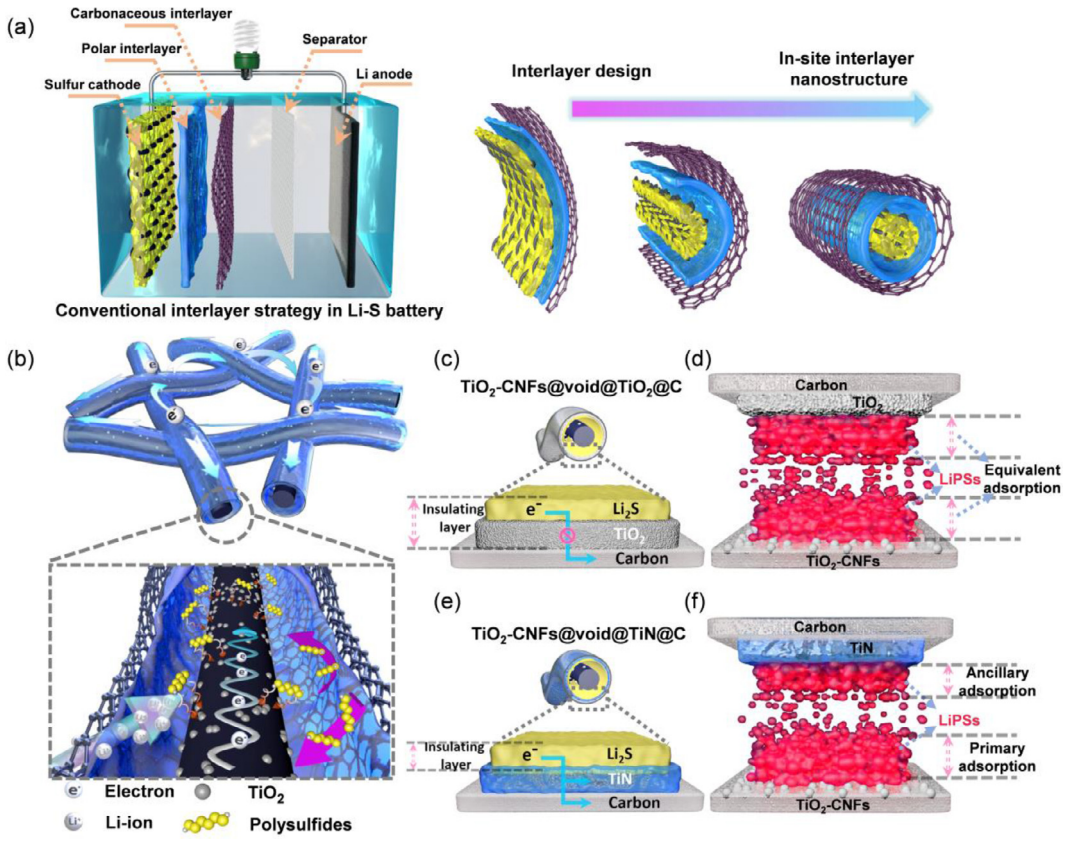

Scheme 1. Design and working principle. Schematic illustration for (a) in-site interlayer design derived from traditional interlayer strategy, (b) working mechanism the TiO_2-CNFs@void@TiN@C/S cathode, (c) interfacial charge transfer of TiO_2@C shell and Li_2S, (d) LiPSs adsorption in the surface of TiO_2-CNFs and TiO_2@C shell, (e) interfacial charge transfer of TiN@C shell and Li_2S, (f) LiPSs adsorption in the surface of TiO_2-CNFs and TiN@C shell.

and mass of batteries caused by the interlayers is also a problem. Therefore, integrating these macro-scale functionalized interlayers into a micro-composite would be an effective strategy to improve the volume utilization of these functional groups while maintaining its original functions in Li-S batteries. As is illustrated in Scheme 1(a), a multilayer nanofiber structure can be constructed based on the traditional multi-interlayer design.

Herein, integrated polar TiN layer and conductive carbon layer in-site over each fiber of TiO_2-CNFs, we designed and synthesized an intact coaxial multilayered hollow TiO_2/carbon nanofibers@void@TiN@carbon (TiO_2-CNFs@void@TiN@C) composite. Each yolk-shell fiber in this TiO_2-CNFs@void@TiN@C composite can be regarded as an electrode unit with two functionalized interlayers (conductive graphitic carbon and polar TiN), and innumerable such electrode units were interwoven into a freestanding membrane that has a high structural uniformity in large scale. As is illustrated in Scheme 1(b), this novel multilayered yolk-shell composite has dual electronic transmission channels consisting of the inner conductive carbon fiber networks and the outer carbon shell. The dual channels can increase the charge transfer efficiency, thereby improving the utilization of sulfur. Besides, the hollow space throughout the whole composite can confine a high content of sulfur and generate substantial contact sites with active materials, which chemically adsorb intermediate LIPSs. The outer carbon shell through the entire skeleton not only provides an in situ physical barrier to inhibit LiPSs shuttles, but moderates the structural collapse caused by volume expansion during the charge-discharge process due to its flexible nature. In order to compensate for the relatively low conductivity of the thin outer carbon shell and to create an inward adsorption for LiPSs, we have selected different polar groups as additives for the shell and yolk of this composite, respectively. The TiO_2 was selected as a polar group to be integrated with the inner CNFs for its stronger adsorption to LiPSs, while the TiN was selected to be combined with the outer carbon shell for its higher conductivity [27–31]. We also synthesized a TiO_2-CNFs@void@TiO_2@C composite which just uses TiO_2 as polar groups for comparison. Scheme 1(c–f) illustrates the functional differences between TiO_2-CNFs@void@TiO_2@C and TiO_2-CNFs@void@TiN@C when they serve as sulfur hosts. As the insulating Li_2S depositing upon the surface of polar sites during the charging process, the TiO_2-CNFs@void@TiO_2@C composite with double insulating layers of TiO_2/Li_2S obviously has a worse electron transfer efficiency than the TiO_2-CNFs@void@TiN@C composite with a single insulating layer of Li_2S. Furthermore, the different LiPSs trapping abilities of TiO_2 and TiN create an adsorption gradient in TiO_2-CNFs@void@TiN@C composite: the primary adsorption effect of the inner TiO_2-CNFs and the ancillary adsorption effect of the outer TiN layer. This adsorption gradient makes the LiPSs concentrate near the TiO_2-CNFs rather than concentrate near the TiN@C shell preferentially and thus alleviating the LiPSs diffusion towards the outside of TiO_2-CNFs@void@TiN@C composite. As for TiO_2-CNFs@void@TiO_2@C composite, the equivalent LiPSs adsorption effect of the shell TiO_2 and yolk TiO_2-CNFs could result in an excessive accumulation of LiPSs near the TiO_2 shell thereby increasing the outward diffusion of LiPSs.

Compared with the previous reports that use the polar TiO_2 or TiN as cathode additives in Li-S batteries for adsorbing LiPSs [31,32], the yolk-shell TiO_2-CNFs@void@TiN@C composite in this work has a designed distribution of polar TiO_2 and TiN, which could improve the utilization of polar sites. Besides, the unique in situ physical block of the intact yolk-shell structure and discrepant adsorption of TiO_2 and TiN for LiPSs constitute a synergetic

effect of entrapping LiPSs. Thus, the cells with as-designed TiO_2-CNFs@void@TiN@C/S composite as a cathode deliver promising comprehensive electrochemical properties even without using any other additive carbon materials.

2. Experimental

2.1. Preparation of TiO_2-CNFs@void@TiN@C/S composite

2.1.1. Synthesis of TiO_2-CNFs and CNFs

The carbon nanofibers film substrate was synthesized in a typical process of electrospinning: 6 mL DMF and 0.5 mL glacial acetic acid were mixed in a conical flask, 1 mL Titanium butoxide was added slowly into the mixture under vigorous stirring and then 1 g PVP was dissolved into the above-solution. The obtained mixture was spun in a typical condition as follows: the flow rate of solution was set to be constant at 1.5 mL h^{-1}; the shift distance of the needle was 6 cm; the receiving distance was kept at 15 cm and the voltage between the aluminum foil receptor and the needle was 15 kV. Besides, an additional solution of 1 g PVP dissolved in 6 mL DMF was spun to obtain a fresh PVP fibers film. The as-collected amorphous TiO_2-PVP and PVP precursor fibers film was dried at 60 °C in vacuum for 12 h, then the paper was pre-heated in an air-circulating oven at 10 °C min^{-1} up to 260 °C for 5 h to stabilize the fiber structure. Subsequently, the stabilized fabric was heated in a tube furnace at 5 °C min^{-1} up to 800 °C for 1 h under the Ar atmosphere. In this process, the TiO_2-PVP fibers and PVP fibers transformed into TiO_2-CNFs and CNFs, relatively.

2.1.2. Synthesis of TiO_2-CNFs@SiO_2

The as prepared TiO_2-CNFs paper was soaked in 6.5 ωt% (1.56 mol L^{-1}) nitric acid solution for 12 h to improve the surface activity of TiO_2-CNFs, and then the paper was washed by deionized water (DW) for several times. After drying out, the activated TiO_2-CNFs paper was soaked in a mixture of 20 mL Isopropanol, 4 mL DW, 2 mL ammonia solution and 2 mL TEOs for 12 h at room temperature. The gray paper of TiO_2-CNFs@SiO_2 was produced via washing with ethanol and DW for several times.

2.1.3. Synthesis of TiO_2-CNFs@void@TiN@C and TiO_2-CNFs@void@TiO_2@C

The in-situ growth of TiO_2 and resorcinol formaldehyde (RF) are in the same way as growing SiO_2 in the paper: the TiO_2-CNFs@SiO_2 paper was immersed in a mixed solution of 20 mL ethanol absolute, 0.1 mL ammonia solution and 0.5 mL titanium butoxide for 12 h at room temperature. After washing and drying, the paper was soaked in a mixture of 20 mL ethanol absolute, 2 mL ammonia solution, 0.2 mL formaldehyde solution and 0.1 g resorcinol overnight. By annealing the above obtained TiO_2-CNFs@SiO_2@TiO_2@RF paper in a tube furnace at 700 °C for 2 h under the NH_3 atmosphere, the TiO_2-CNFs@SiO_2@TiN@C were fabricated. Subsequently, the TiO_2-CNFs@SiO_2@TiN@C paper was soaked in a NaOH solution (0.25 mol L^{-1}) overnight to etch the intermediary SiO_2 layer out and then the paper was washed by DW of 60 °C. After drying out, the TiO_2-CNFs@void@TiN@C composite was obtained. The TiO_2-CNFs@void@TiO_2@C composite was synthesized under the same condition but change the annealing atmosphere into Ar.

2.1.4. Synthesis of TiO_2-CNFs@void@TiN@C/S

Firstly, the paper-like TiO_2-CNFs@void@TiN@C film was cut into wafers with a diameter of 12 mm, and then an S/carbon disulfide (CS_2) solution was prepared by dissolving S into CS_2 with the concentration of 0.1 g mL^{-1}. Subsequently, the TiO_2-CNFs@void@TiN@C wafers ware soaked into the as-prepared solution for 10 h and then dried in a fume hood. Finally, the wafers were put into different teflon-lined autoclaves and kept at 155 °C for 12 h to ensure that the S is fully impregnated into the TiO_2-CNFs@void@TiN@C. By the way, the wafers were weighed before and after sulfur incorporation to calculate the sulfur loading. In this way, a cathode of TiO_2-CNFs@void@TiN@C/S composition was obtained, and TiO_2-CNFs@void@TiO_2@C/S, TiO_2-CNFs/S and CNFs/S cathodes were synthesized by the same process.

2.2. Material characterization

The morphology and microstructure of the as-obtained composite were characterized using field-emission scanning electron microscopy (SEM, ZEISS SIGMA 500) and transmission electron microscopy (TEM, FEI Tecnai G20) equipped with energy-dispersive X-ray spectroscopy (EDX). X-ray diffraction (XRD, Rigaku Ultima IV (Cu K_α radiate on, λ = 1.5418 Å)) and X-ray photoelectron spectroscopy (XPS, AXIS Supra) were employed to analyze the phase and component of the above samples. Thermogravimetric analysis (TGA, SDTQ600) was conducted to determine the sulfur content in the composites. The N_2 adsorption-desorption curves were evaluated using Micromeritics ASAP 2460 analyzer after degassing the samples at 300 °C under vacuum for 6 h. The average pore distribution was calculated using Density Functional Theory models and Barrett-Joyner-Halenda models for micropores and mesopores, respectively. The electrical conductivity of the samples is determined by using a standard four-point-probe resistivity measurement system (ST2263, Suzhou, China).

2.3. Electrochemical measurements

The as-prepared small disk of TiO_2-CNFs@void@TiN@C/S, TiO_2-CNFs@void@TiO_2@C/S, TiO_2-CNFs/S and CNFs/S composites are used directly as electrodes without any additives. The typical mass loading of active S in the electrode was 1.5–2 mg cm^{-2}. To prepare an electrode with a higher sulfur mass loading, the thin TiO_2-CNFs@void@TiN@C/S films were stacked into a relatively thick electrode with 20 μL conductive slurry (10 mg Super P and 10 mg PVDF mixed in 2 mL NMP) added in the surface of each TiO_2-CNFs@void@TiN@C/S film. The coin-like 2025 type cells were assembled with the above electrodes as the cathode and lithium foils as the anode. DOL/DME (1:1, v/v) with 1 M LiTFSI (lithium bis(trifluoromethane sulfonimide)) and 0.1 M $LiNO_3$ were used as the electrolyte and Celgard 2400 film as a separator. The ratio of electrolyte to sulfur was controlled as 20 μL mg^{-1} (the cell with a single electrode) and 5 μL mg^{-1} (the cell with a stacked electrode), and all cells were prepared in an Ar-filled dry box (NOBODY). The cyclic voltammetry measurements (CV) and the electrochemical impedance spectroscopy (EIS) measurements were performed via a CHI660E electrochemical workstation. The scanning rate and voltage range of CV measurements were 0.1 mV/s and 1.7–2.7 V, respectively. The EIS measurements began at the open-circuit potential in the frequency range between 10 mHz and 200 kHz. The galvanostatic charge and discharge measurement were carried out by a Land CT2001A battery analyzer in the voltage range 1.7–2.7 V. For symmetric cells, the test samples were cutting into small wafers as electrodes, and the two electrodes in each cell have the similar weight. 30 µL special electrolyte was added into the cell, and the special electrolyte was composed of 1 M LiTFSI, 0.1 M $LiNO_3$ and 0.2 M Li_2S_6 in DOL and DME (1:1, v/v). The CV curves of the symmetrical cells were performed within a voltage window of −1 to 1 V at a scan rate of 5 mV s^{-1}.

Adsorption Test of LiPSs: As a representative of the soluble polysulfide species, Li_2S_6 was synthesized by chemically reacting sulfur and Li_2S in a mixture of 1,2-dimethoxyethane (DME) 1,4-dioxane (DOL) in an Ar-filled glove box: 50 mL DME and 50 mL

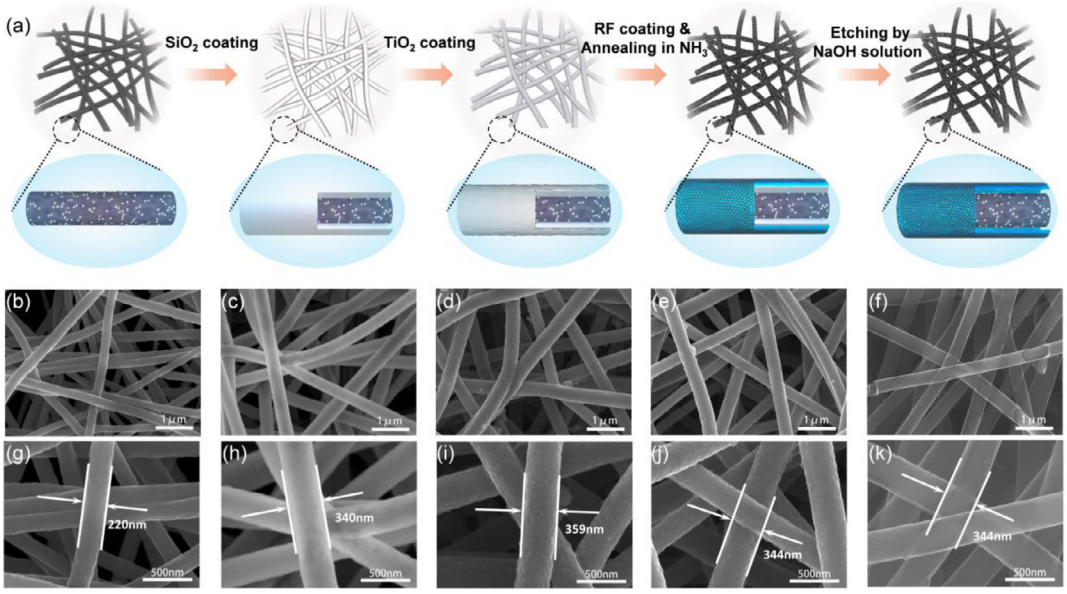

Fig. 1. Synthesis process of the TiO_2-CNFs@void@TiN@C composite. (a) Schematic illustration of the synthesis process of the TiO_2-CNFs@void@TiN@C composite. SEM images of (b, g) TiO_2-CNFs, (c, h) TiO_2-CNFs@SiO_2, (d, i) TiO_2-CNFs@SiO_2@TiO_2, (e, j) TiO_2-CNFs@SiO_2@TiN@C and (f, k) TiO_2-CNFs@void@TiN@C. Scale bars, 1 μm (b–f); scale bars, 500 nm (g–k).

DOL were mixed in a glass bottle, and then 23 mg lithium sulfide (Li_2S) and 80 mg sulfur (molar ratio of 1:5) were added into the mixture. After 10 h of vigorous stirring, a Li_2S_6 solution (5 mmol L^{-1}) was obtained. 5 mL of the Li_2S_6 solution was mixed with 15 mg crushed test samples (TiO_2-CNFs@void@TiN@C, TiO_2-CNFs@void@TiO_2@C, TiO_2-CNFs and CNFs).

3. Results and discussion

3.1. Materials synthesis and characterization

Fig. 1(a) illustrates the synthesis of TiO_2-CNFs@void@TiN@C. First, a TiO_2-CNFs film was synthesized by a typical electrospinning method and the subsequent carbonization. As shown in the scanning electron microscope (SEM) images in Fig. 1(b, g), the TiO_2-CNFs have a relatively uniform fiber diameter of about 220 nm. The layer of SiO_2 was then coated on the surface of the TiO_2-CNFs by a method of hydrolysis, which makes the nanofibers look obviously thicker than before (Fig. 1c, h). The TiO_2-CNFs@SiO_2 maintain a complete nanostructure of nanofibers, and the SiO_2 layer can be clearly distinguished from the TiO_2-CNFs substrate at the fracture of nanofibers in the SEM image (Fig. S1). In a same way, a TiO_2 layer and a resorcinol formaldehyde (RF) layer were coated on the as-prepared nanofibers in sequence. And then the multilayer nanofibers were heated at 700 °C in NH_3 atmosphere, in which course the outer amorphous TiO_2 transformed into TiN and the RF layer was carbonized (Fig. 1d, e, i, j). Finally, the SiO_2 in the middle layer was removed by a dilute NaOH solution to obtain a hollow TiO_2-CNFs@void@TiN@C host material (Fig. 1f, k).

In Fig. 2(a), the TiO_2-CNFs@void@TiN@C showed a well-maintained coaxial tubular structure and the inner hollow space between TiN layer and TiO_2-CNFs can be clearly seen in the section of the nanofibers. Moreover, after a series of synthesis processes, the final product TiO_2-CNFs@void@TiN@C composite still maintains an intact appearance of a freestanding film (Fig. S2a) and its structural integrity can be attributed to the good flexibility of TiO_2-CNFs. As shown in Fig. S2(b), the films of TiO_2-CNFs and TiO_2-CNFs@void@TiN@C were still intact after folding while the CNFs film was broken into two parts, indicating the increased mechanical robustness through TiO_2 addition. By the way, as measured by micrometer, the average thickness of the TiO_2-CNFs@void@TiN@C is about 50 μm, without any increase compared with its precursor TiO_2-CNFs. Compared with the morphology of TiO_2-CNFs@void@TiN@C, the TiO_2-CNFs@void@TiN shows a very irregular surface and the TiN layer has many defects (Fig. S3). It indicates that the outer carbon film can provide an attachment for the TiO_2 layer to homogeneously convert into TiN without cracking and shedding, and this is essential to fabricate an intact TiN shell. In the X-ray photoelectron spectroscopy (XPS) results (Fig. 2b, c), the Ti 2*p* spectra of TiO_2-CNFs@void@TiN@C show three types peaks, which is attributed to Ti-O bond (464.4 and 458 eV), Ti−N−O bond (462.9 and 457.2 eV) and main Ti−N bond (461.2 and 456 eV). Although there is a low content of O in Ti−N−O and Ti−O, the main ingredient of the outer layer is TiN phase, which is consistent with previously reported TiN-based materials [32–35]. In addition, the three peaks at 395.1, 397.3 and 399.2 eV of the N 1*s* spectra can be assigned to the C−N, Ti−N, and Ti−N−O bond, respectively [36]. The survey XPS spectra of TiO_2-CNFs@void@TiN@C and TiO_2-CNFs were compared in Fig. S4, the spectra of TiO_2-CNFs@void@TiN@C show an extra peak of N 1*s* and a higher relative intensity of C 1*s* peak, which are attributed to its extra TiN@C shell compared with TiO_2-CNFs. Meanwhile, the Ti 2*p* spectra of TiO_2-CNFs only show two typical peaks which are originating from the Ti $2p_{3/2}$ and Ti $2p_{1/2}$, highly consistent with the previously reported TiO_2 composite [37–39].

The TEM images (Fig. 2d, e, g) further prove the double-shell hollow structure (as is illustrated in Fig. 2i) of TiO_2-CNFs@void@TiN@C composite, and the fine crystal particles of TiN are uniformly distributed on the inner surface of the ultra-thin carbon layer. From the High resolution TEM (HRTEM) observations (Fig. 2f, h), it can be found that the lattice fringes of the shell-layer are correlated to the (200) planes of TiN and the lattice fringes of the inner TiO_2-Carbon nanofibers are correlated to the (110) planes of rutile TiO_2. Fig. 2(j) shows the X-ray diffraction patterns of the as-prepared TiO_2-CNFs@void@TiN@C, it can be clearly observed that the TiO_2-CNFs@void@TiN@C consists of TiO_2 and TiN phase. The HRTEM results are highly consistent with the XRD results and they prove that the crystal phase of TiN was successfully generated in the shell-layer while the rutile TiO_2 in the inner carbon nanofibers maintains the original crystal phase.

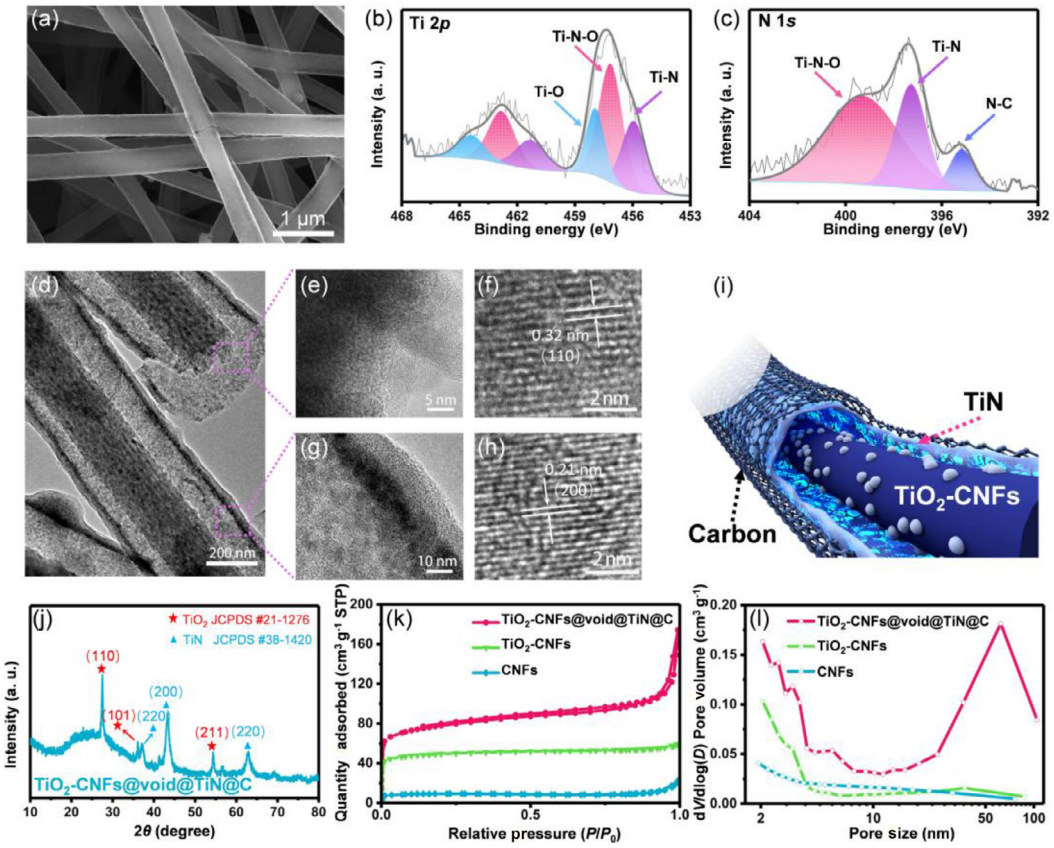

Fig. 2. Characterization of TiO_2-CNFs@void@TiN@C. (a) SEM image, (b) XPS Ti 2*p* spectra, (c) XPS N 1*s* spectra, (d, e, g) TEM images, (f, h) HRTEM images, (i) schematic illustration of the coaxial multilayered hollow structure, and (j) X-ray diffraction patterns of TiO_2-CNFs@void@TiN@C. (k) Nitrogen adsorption/desorption isotherms and (l) pore size distribution of CNFs, TiO_2-CNFs and TiO_2-CNFs@void@TiN@C.

Additionally, some TiO_2-CNFs used as the precursor were heated together with the TiO_2-CNFs@SiO_2@TiO_2@RF in NH_3 atmosphere to see the stability of the crystallized rutile TiO_2 in the TiO_2-CNFs. And the result shows that there was no transition occurred on the TiO_2-CNFs during the annealing process (Fig. S5).

From an artificially damaged part of TiO_2-CNFs@void@TiN@C (Fig. S6a), it can be found that the outer carbon layer was distinctly different from the TiN layer and it seems like a protective film wrapping the inner TiN perfectly. Different from the smooth surface of the outer carbon layer, the inner TiN layer shows a rough surface, which is consisted of fine TiN nanoparticles. And this means that the inner surface has a better sulfur affinity than the outer surface. To show the suitability of the TiO_2-CNFs@void@TiN@C composite for sulfur loading, the hollow space in the composite was simply quantified. In a discovered broken fiber, where the inner TiO_2-CNFs and the outer TiN shell could be clearly distinguished (Fig. S6b), the diameter of TiO_2-CNFs and the inner diameter of TiN shell were measured. After simple calculations, it can be found that the hollow space in the yolk-shell nanofibers is approximately equivalent to a nanotube with an inner diameter of 245 nm (Fig. S6c). Nitrogen physisorption analysis shows that the Brunauer-Emmett-Teller (BET) surface area of TiO_2-CNFs@void@TiN@C is 257.3 $m^2\ g^{-1}$, which is almost 100 $m^2\ g^{-1}$ higher than the 159.2 $m^2\ g^{-1}$ of TiO_2-CNFs and 10 times higher than the 25.1 $m^2\ g^{-1}$ of the CNFs (Fig. 2k). Meanwhile, the TiO_2-CNFs@void@TiN@C have a bimodal pore size distribution, and the extra peak at 62 nm highly matches its morphological structure. The large hollow space in the TiO_2-CNFs@void@TiN@C composite makes it possible to load a large amount of sulfur and accommodate the volumetric expansion of sulfur during lithiation.

Sulfur was composited with TiO_2-CNFs@void@TiN@C by a modified melt-diffusion method usually used in Li-S batteries [40–42]. After sulfur diffusion, the as-prepared TiO_2-CNFs@void@TiN@C/S composite showed the same nanofiber structure as its original host, and there was no sulfur remained outside of the TiO_2-CNFs@void@TiN@C host (Fig. S7). The X-ray diffraction pattern of TiO_2-CNFs@void@TiN@C/S (Fig. 3a) shows an intensive diffraction peak of sulfur, and the characteristic peak of TiO_2 and TiN phase can be also found. The X-ray (EDX) spectrum (Fig. 3b) of the TiO_2-CNFs@void@TiN@C/S composite also shows an intensive peak of element sulfur, which is even stronger than the peak of element carbon. The TGA result (Fig. 3c) shows that the TiO_2-CNFs@void@TiN@C/S composite has a high sulfur content of 68 wt%. From the SEM observations and the associated EDX elemental distributions of TiO_2-CNFs@void@TiN@C/S composite (Fig. S8), it can be observed that sulfur is homogeneously distributed along the fiber and there is no sulfur particle outside the fiber. The magnified nanofiber image and its corresponding linear/area elemental distributions (Fig. 3d) further confirmed that the sulfur was melted in the hollow space between TiN layer and the inner TiO_2-CNFs.

3.2. Electrochemical performance

The electrochemical performance of TiO_2-CNFs@void@TiN@C/S as a cathode material for Li-S batteries was evaluated. In order to interpret the rationality of this TiN@TiO_2 structure design, a TiO_2-CNFs@void@TiO_2@C composite was fabricated by a similar process only changes the final annealing atmosphere into Ar. Sulfur was composited with TiO_2-CNFs@void@TiO_2@C, TiO_2-CNFs and

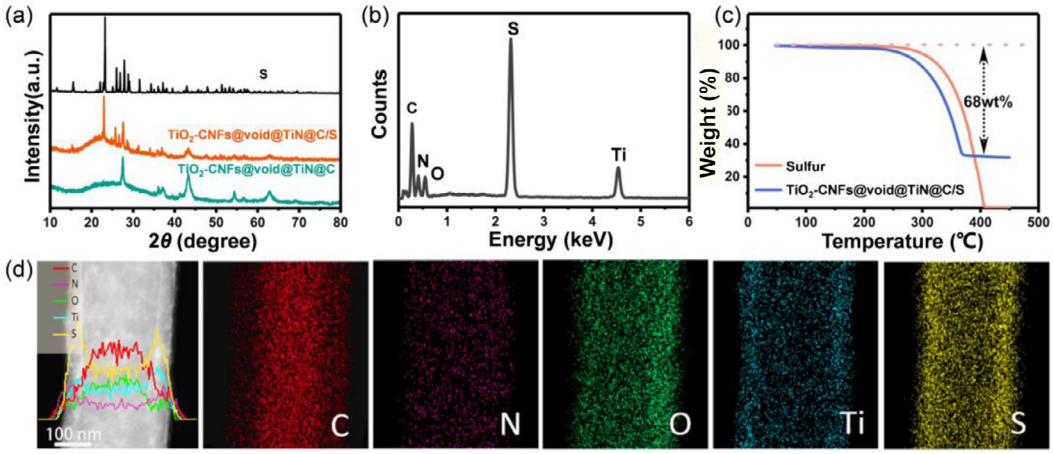

Fig. 3. Characterization of S/TiO_2-CNFs@void@TiN@C. (a) X-ray diffraction patterns of sulfur, TiO_2-CNFs@void@TiN@C and TiO_2-CNFs@void@TiN@C/S. (b) EDX spectrum, (c) TGA curves, (d) TEM image, linear elemental distributions and area elemental distributions for C, N, O, Ti and S, of TiO_2-CNFs@void@TiN@C/S.

CNFs by a same method as TiO_2-CNFs@void@TiN@C/S cathode. And the all four samples were assembled into coin cells in a same mass loading of sulfur. From the Nyquist plots (Fig. 4a), it can be found that TiO_2-CNFs@void@TiN@C/S cathode has the smallest semicircle in high-frequency region, which means the minimum charge transfer resistance among all samples [43–45]. It indicates that the hollow and double charge channel structure improved the charge transfer among the cathode and the electrolyte, thereby effectively expediting the utilization of sulfur. Unexpectedly, the TiO_2-CNFs@void@TiO_2@C/S cathode has a much larger semicircle than the other three samples, it means the worst conductivity in all four cathodes. As measured in the four-point-probe resistivity measurement system, the electrical conductivities of TiO_2-CNFs@void@TiO_2@C is 1.06×10^{-2} S cm^{-1}, much lower than the 2.73 S cm^{-1} of the TiO_2-CNFs@void@TiN@C. And this indicates that the outer TiO_2 layer in the TiO_2-CNFs@void@TiO_2@C/S cathode acts as a complete insulating layer, which is undesirable in Li-S batteries. Besides, the TiO_2-CNFs/S electrode also has a large semicircle than the CNFs/S electrode, manifesting that the charge transfer ability of TiO_2-CNFs/S electrode is poorer than CNFs/S electrode, which is obviously attributed to the relatively low conductivity of TiO_2. In the low-frequency region, the inclined line is associated with the Warburg impedance [32], and the slope of CNFs/S electrode is obviously larger than the others, which might be due to the lack of the active spots and the lower specific surface area.

From the CV profiles of the four electrodes, it can be found all of the four cathodes present two cathodic peaks, corresponding to the two-step reduction of sulfur to Li_2S_2/Li_2S. In the anodic scan, the CNFs/S electrode shows only one anodic peak while the other three electrodes present two anodic peaks, the extra anodic peak could be attributed to the catalytic effect of the polar sites on the conversion of insoluble Li2S/Li2S into high-order soluble lithium polysulfides [26]. It is noteworthy that the TiO_2-CNFs@void@TiN@C/S cathode displays well-defined redox peaks with higher peak currents while the TiO_2-CNFs@void@TiO_2@C/S cathode displays bulging redox peaks with the lowest peak currents, indicating that TiO_2-CNFs@void@TiN@C/S cathode has a rapid conversion kinetics, which is ascribed to its high conductivity. Besides, the CV curves of TiO_2-CNFs@void@TiN@C/S cathode in the first three cycles shown in Fig. S9 are well overlapped, confirming an excellent electrochemical reversibility.

The rate capabilities and electrode kinetics of these cathode materials were demonstrated in Fig. 4(d), the cell with TiO_2-CNFs@void@TiN@C/S as a cathode exhibits obvious excellent rate performance in which the discharge capacities are stabilized around 1482.3, 1249.9, 1106, 1024.3, 929.3 and 688.5 mAh g^{-1} at 0.1, 0.2, 0.5, 1, 2 and 5 C (1 C = 1675 mA g^{-1}), respectively. When it occurs to TiO_2-CNFs/S and CNFs/S electrodes, abrupt capacity drop can be found in the first few cycles, indicating a poor ability to restrain LIPSs. The capacity of TiO_2-CNFs@void@TiO_2@C/S cathode drops dramatically to 117 mAh g^{-1} as the current density rises up to 1 C, indicating the poor conductivity of the compact TiO_2 layer as the Nyquist plots shows. When the current density is reduced back to 0.5 C, the discharge capacity of TiO_2-CNFs@void@TiN@C/S is recovered to 1103.5 mAh g^{-1}, and it also retains a relatively stable trend in the next 170 cycles. After the all 200 cycles, the discharge capacity of TiO_2-CNFs@void@TiN@C/S also retains a relatively high value of 941.2 mAh g^{-1}, while the discharge capacity of TiO_2-CNFs@void@TiO_2@C/S, TiO_2-CNFs/S and CNFs/S electrodes drop to 562.6, 499 and 287.6 mAh g^{-1}, respectively, indicating that the hollow structure and inner polar sites of TiO_2-CNFs@void@TiN@C promise better entrapment for the LIPSs. Additionally, the TiO_2-CNFs@void@TiO_2@C/S electrode shows a better capacity retention rate than TiO_2-CNFs/S cathode, and this improvement may be attributed to the multilayered hollow of TiO_2-CNFs@void@TiO_2@C composite. The galvanostatic charge-discharge profiles of TiO_2-CNFs@void@TiN@C/S at various current rates are shown in Fig. 4(c). It can be found that all the profiles have two discharge plateaus and one well-defined charge plateau with high coulombic efficiency even the current density increased to 5 C.

Fig. 4(e) shows the long cycling performance of TiO_2-CNFs@void@TiN@C/S, TiO_2-CNFs/S and CNFs/S electrodes with the same sulfur mass loading of 1.5–2 mg cm^{-2} at 1 C rate after the initial one activation process in smaller current density (0.2 C). Obviously, the TiO_2-CNFs@void@TiN@C/S cathode shows the highest initial specific capacity of 1110.3 mAh g^{-1} (1 C) and the lowest average decay rate of 0.054% per cycle. After 1000 charge/discharge cycles at 1 C, a capacity of 675.8 mAh g^{-1} is still available with the TiO_2-CNFs@void@TiN@C/S cathode, highly overmatching the capacity of TiO_2-CNFs/S and CNFs/S cathodes, further demonstrating the effective inhibition of the dissolution and shuttle effect of the coaxial TiO_2-CNFs@void@TiN@C hollow structure during cycling. Benefitting from the high conductivity of the CNFs, the CNFs/S electrode delivers a higher capacity than the TiO_2-CNFs/S electrode in the first few cycles of 1 C. However, after 400 cycles, the discharge capacity of CNFs/S cathode drops to 244 mAh g^{-1} while TiO_2-CNFs/S cathode still delivers a capacity of 545 mAh g^{-1}. Compared with CNFs/S cathode, the relatively good cyclic stability of TiO_2-CNFs/S cathode is attributed to the chemical adsorption of polar TiO_2 to LIPSs, and this is consistent

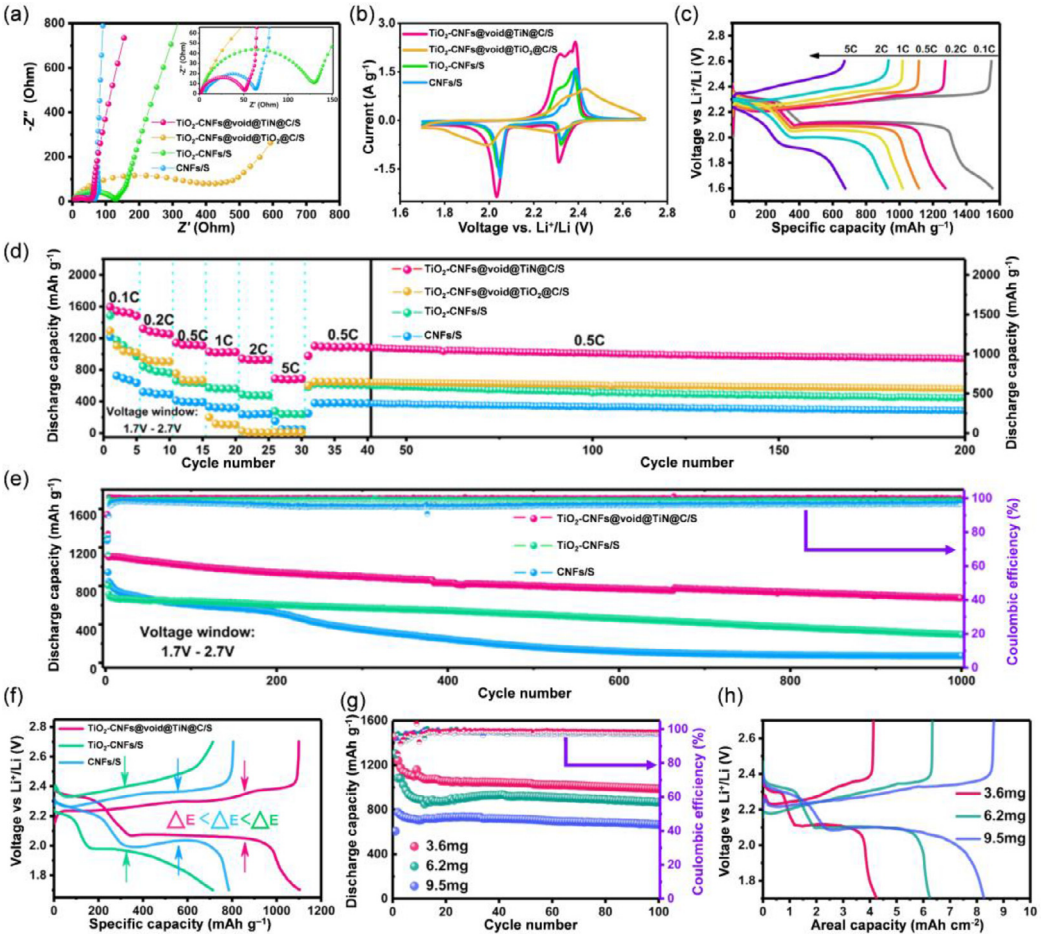

Fig. 4. Electrochemical evaluation. (a) Nyquist plots before cycling from 0.1 MHz to 20 mHz, (b) CV curves at a scan rate of 0.1 mV s^{-1} in a potential window from 1.7 to 2.7 V of CNFs/S, TiO_2-CNFs/S, TiO_2-CNFs@void@TiO_2@C/S and TiO_2-CNFs@void@TiN@C/S cathodes. (c) Galvanostatic charge-discharge profiles of the cell with TiO_2-CNFs@void@TiN@C/S cathode at various current densities from 0.1 to 5 C. (d) Rate capabilities and the subsequent cycle performance of CNFs/S, TiO_2-CNFs/S, TiO_2-CNFs@void@TiO_2@C/S and TiO_2-CNFs@void@TiN@C/S cathodes. (e) Long cycling performance and (f) the corresponding second-cycle galvanostatic charge/discharge voltage profiles of TiO_2-CNFs@void@TiN@C/S, TiO_2-CNFs/S, CNFs/S cathodes at 1 C rate. (g) Cycling performance and (h) the corresponding second-cycle galvanostatic charge/discharge voltage profiles of TiO_2-CNFs@void@TiN@C/S electrodes with S areal loadings of 3.6, 6.2 and 9.5 mg cm^{-2} at a current density of 1.5 mA cm^{-2}.

with the former research [21]. Fig. 4(f) shows the second-cycle galvanostatic charge/discharge voltage profiles of the CNFs/S, TiO_2-CNFs/S and TiO_2-CNFs@void@TiN@C/S cathodes at 1 C. All three samples have two discharge plateaus at ~2.3 V (corresponding to the reduction of sulfur to long-chain LIPSs) and ~2.1 V (the formation of short-chain LIPSs). And among these, the two discharge plateaus of TiO_2-CNFs@void@TiN@C/S are not only the highest but also the longest, suggesting more efficient utilization of sulfur in TiO_2-CNFs@void@TiN@C/S. Furthermore, compared with the TiO_2-CNFs/S and CNFs/S, the TiO_2-CNFs@void@TiN@C/S cathode also exhibits the lowest voltage hysteresis (ΔE), which means a lower polarization and excellent electrochemical reaction kinetics.

Since high mass loading of active materials and high areal capacities are essential for the energy density of Li-S batteries [46], the thin TiO_2-CNFs@void@TiN@C/S films are stacked into a relatively thick electrode to achieve a high areal sulfur mass loading. After stacked 2, 3 and 5 layers of TiO_2-CNFs@void@TiN@C/S films, the TiO_2-CNFs@void@TiN@C/S electrodes with areal sulfur loading of 3.6, 6.2 and 9.5 mg cm^{-2} were obtained, respectively. The total sulfur contents in the stacked electrodes were calculated to be about 62 wt%, and the thicknesses of the stacked films with 2, 3 and 5 layers were measured as 100, 170 and 300 μm, respectively. As is shown in Fig. 4(g), at a current density of 1.5 mA cm^{-2}, with the sulfur loadings of 3.6, 6.2, and 9.5 mg cm^{-2}, the cells exhibit discharge capacities of, respectively, 1240.2, 1083.4, and 775.1 mAh g^{-1}. After 100 cycles, the reversible discharge capacities maintain at, respectively, 987.5, 868.7, and 668.5 mAh g^{-1}, achieving a high capacity retention rate of 79%–86%. Fig. 4(h) shows the second-cycle galvanostatic charge/discharge voltage profiles of the three cathodes with different sulfur loading. It could be found that each of the three cathodes delivers a high discharge plateaus at 2.1 V, suggesting that the stacking process has excellent applicability with the TiO_2-CNFs@void@TiN@C/S cathode. Moreover, the areal capacity of the electrode with areal sulfur loading of 9.5 mg cm^{-2} could achieve up to 8.2 mAh cm^{-2}, which is comparable to the current available Li-ion cell (4 mAh cm^{-2}) [47].

In order to further explore the reason for the improved performance of the TiO_2-CNFs@void@TiN@C/S cathode, the cyclic voltammetry of the symmetric cells as well as those without the Li_2S_6 were measured at a scan rate of 5 mV s^{-1}. The TiO_2-CNFs@void@TiO_2@C, TiO_2-CNFs, and CNFs prepared under the same condition were used as the experimental controls. In Fig. 5(a), two distinct pairs of sharp redox peaks can be observed for the TiO_2-CNFs@void@TiN@C composite with Li_2S_6 electrolyte. The two cathodic peaks located at 0.06 and 0.25 V represent the oxidation of Li_2S to Li_2S_6 and Li_2S_6 to sulfur on working electrode. In the reversed process, the reduction of S to Li_2S can be revealed through the two reduction peaks at −0.06 and −0.25 V [48]. Besides, the TiO_2-CNFs cell shows a larger potential hysteresis with two pairs of broader redox peaks at −0.3/0.3 and −0.6/0.6 V,

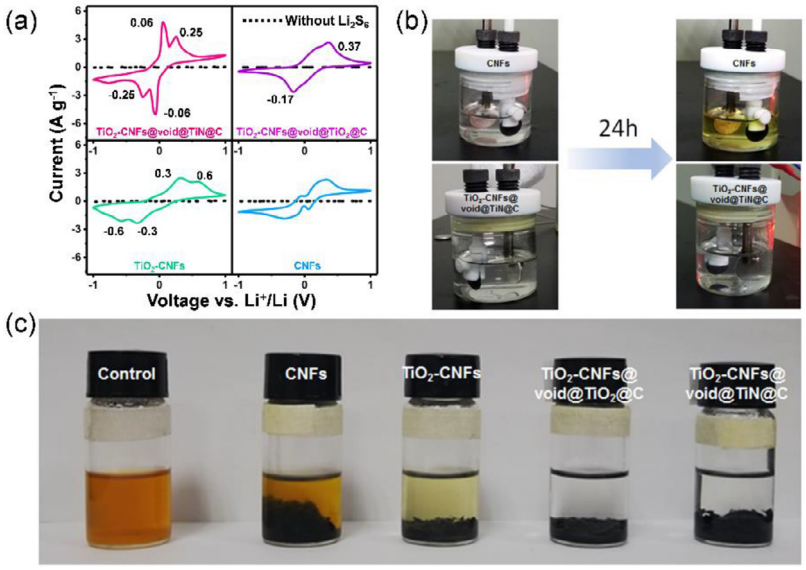

Fig. 5. Adsorption measurements. (a) CV curves of Li_2S_6 and Li_2S_6-free symmetric batteries of TiO_2-CNFs@void@TiN@C, TiO_2-CNFs@void@TiO_2@C, TiO_2-CNFs and CNFs electrodes. (b) Optical observation of transparent cells of CNFs/S and TiO_2-CNFs@void@TiN@C/S cathodes. (c) Optical observation of Li_2S_6 adsorption by CNFs, TiO_2-CNFs, TiO_2-CNFs@void@TiO_2@C and TiO_2-CNFs@void@TiN@C after 24 h.

while the cell based on TiO_2-CNFs@void@TiO_2@C suffers from even more severe polarization with only two asymmetric peaks at −0.17 and 0.37 V. Among all of the four samples, the TiO2-CNFs@void@TiN@C shows the highest current density and the smallest peak separation in the CV curves, indicating the better catalytic effect on electrochemical conversion of LiPS.

Fig. 5(b) shows the operando photographs of transparent vial cells. In a galvanostatic charge-discharge process with a current of 0.1 mA, the electrolyte in the CNFs/S vial cell turns yellow after 24 h while the electrolyte in the TiO_2-CNFs@void@TiN@C/S vial cell remained transparent. With the extreme diffusion of LIPSs into the electrolyte, the discharge capacity of the CNFs/S vial cell decreases rapidly. At the same condition, the TiO_2-CNFs@void@TiN@C/S vial cell maintains a relatively high specific capacity (Fig. S10) and its electrolyte color changes little after 10 cycles (Fig. S11), implying that the high affinity of TiN/TiO_2 nanoparticles and the strong restriction of the multilayered hollow structure prevent the dissolution of soluble LIPSs.

In the adsorption test (Fig. 5c), Li_2S_6 was expressed as a representative species of LIPSs. The visual observation shows that the solutions in both of the TiO_2-CNFs@void@TiO_2@C vial and the TiO_2-CNFs@void@TiN@C vial are colorless, indicating an equal efficacy in adsorbing LIPSs of the two samples. Besides, the Li_2S_6/TiO_2-CNFs solution shows a color decay for the chemical interaction between TiO_2 nanoparticles and Li_2S_6, while the Li_2S_6/CNFs solution remains a bright yellow color. Compared with the CNFs and TiO_2-CNFs, the stronger Li_2S_6 adsorption performance of TiO_2-CNFs@void@TiN@C and TiO_2-CNFs@void@TiO_2@C could be attributed to their larger surface area and more adsorption sites under the same mass.

The above-presented results demonstrate that the TiO_2-CNFs@void@TiN@C/S cathode performs excellent not only in rate capacity and cycling ability but also in achieving a high sulfur mass loading. Compared with the TiO_2-CNFs and CNFs composites which belong to traditional single fibrous materials, the excellent performance of TiO_2-CNFs@void@TiN@C composite as a Li-S battery cathode mostly attribute to the unique coaxial yolk-shell structure with the polar TiN and TiO_2 homogeneously distributed throughout the inner surface. Previous studies have also revealed these structural advantages of yolk-shell materials in sulfur electrode [11,14,49–53] and the polar TiN and TiO_2 materials have been proved to be suitable additive for improving the performance of the sulfur electrode. This TiO_2-CNFs@void@TiN@C composite integrates the yolk-shell structure to an intact freestanding CNFs-based film and forms a coherent pipeline structure. Nevertheless, the TiO_2-CNFs@void@TiO_2@C composite with this unique structure shows little superiority over the TiO_2-CNFs composite when they serve as sulfur hosts: The TiO_2-CNFs@void@TiO_2@C/S cathode shows a poor conductivity and subsequently performs weakly in rate capacity. This adverse effect in cell performance can be attributed to the incrassate insulating layer in TiO_2-CNFs@void@TiO_2@C cathode. The insulating TiO_2 in the TiO_2@C shell exists as an independent layer and lacks effective contact with the conductive carbon, the absorbed LiPSs in the TiO_2 surface cannot convert quickly due to the limited charge transfer efficiency [54]. Besides, the initial sulfur and the later generated Li_2S are deposited in the surface of the TiO_2 layer, leading to a further drop in conductivity. The incrassate insulating layer of TiO_2/Li_2S impedes the electron transfer between the conductive network and the active materials while the excellent conductivity of TiN layer can accelerate the charge transfer, demonstrating that structural design should also take a consideration of the compatibility of different materials. Furthermore, the different binding energy of the TiN shell and TiO_2 yolk to the intermediate LiPSs can prevent the excessive deposition of Li_2S on the TiN surface, thereby avoiding the deterioration of conductivity and the loss of active materials [27,30].

The working mechanism of the TiO_2-CNFs@void@TiO_2@C composite as a sulfur host can be summarized as follows: The inner TiO_2-CNFs with large length/diameter ratio are easy to form a 3D network for the composite, which can not only facilitate the electron and ion transport for sulfur reactions but also provide sufficient polar TiO_2 sites for adsorbing polysulfides, thus ensuring a high utilization rate of sulfur. In addition, the TiN@C layers construct a hollow structure with the polar TiN in the inner surface, and this hollow structure can provide sufficient voids for accommodating the volume change of the inner sulfur during cycling. Furthermore, the TiN layer not only serves as a polar material in chemically adsorbing LiPSs but also improves the conductivity of the outer carbon layer. The double charge channel constructed by the outer carbon shell and the inner carbon fiber can significantly reduce the conductivity decrease caused by the introduction of the polar TiO_2, which has poor conductivity but plays an impor-

tant role in entrapping polysulfides. During the charge-discharge process, the soluble polysulfide intermediates were sandwiched between TiN layer and TiO_2-CNFs, while the Li^+ ions can pass through the TiN@C shell. Under the physical confinement of the TiN@C shell and the chemical adsorption of the polar TiN/TiO_2 to polysulfides, the TiO_2-CNFs@void@TiN@C/S cathode delivers a remarkable electrochemical performance as presented in the above results. Moreover, the freestanding TiO_2-CNFs@void@TiN@C/S cathode eliminate the use of harsh slurry-cast processes in battery assembly. If including all parameters (sulfur/electrolyte ratio, sulfur loading, the weight of Al-foil, binders, conducting additives), this TiO_2-CNFs@void@TiN@C/S cathode manifested the advantages of fabricating freestanding architectures (see Table S1) of such polar materials for next-generation Li-S batteries.

4. Conclusions

In summary, we have synthesized a freestanding coaxial hollow TiO_2-CNFs@void@TiN@C composite by a facile and reliable hard-templating method. Sulfur was infused into the hollow space of the TiO_2-CNFs@void@TiN@C composite to fabricate a TiO_2-CNFs@void@TiN@C/S cathode for Li-S batteries. In the unique structure of TiO_2-CNFs@void@TiN@C composite, the inner CNFs acts as a structurally stable conductive backbone to transport electrons for the charge-discharge reactions, the TiO_2 nanoparticles and TiN layer can chemically adsorb polysulfide and suppress the shuttle effect during the charge-discharge process, and the outer carbon layer serves as a flexible barrier to prevent the outward diffusion of polysulfide intermediates. Therefore, the TiO_2-CNFs@void@TiN@C/S cathode exhibits better active material utilization and electrochemical reversibility than the TiO_2-CNFs/S and CNFs/S cathodes. The TiO_2-CNFs@void@TiN@C/S cathode with a sulfur content of 68 wt% displays an initial discharge capacity of 1110.3 mAh g^{-1} and a reversible discharge capacity of 675.8 mAh g^{-1} after 1000 cycles at 1 C charge-discharge rate. Besides, the high capacity of 688.5 mAh g^{-1} is obtained even at a high current density of 5 C. More importantly, the sulfur loading of TiO_2-CNFs@void@TiN@C/S cathode could be further increased to 9.5 mg cm^{-2}, resulting in a high areal capacity of 8.2 mAh cm^{-2}. Consequently, we believed that TiO_2-CNFs@void@TiN@C fabricated in this work not only can provide insights on the high-performance Li–S batteries, but also would present a novel idea in structural design, in which the yolk-shell structure is introduced into a freestanding carbon film and construct a complete 3D network pipeline.

Declaration of Competing Interest

The authors declare that they have no conflict of interest.

Acknowledgments

The work was supported by the National Natural Science Foundation of China (Nos. 51972287, 51502269), Natural Science Foundation of Henan Province (No. 182300410187) and Outstanding Young Talent Research Fund of Zhengzhou University (No. 1521320023).

Supplementary materials

Supplementary material associated with this article can be found, in the online version, at doi:10.1016/j.jechem.2020.03.065.

References

[1] X.L. Ji, K.T. Lee, L.F. Nazar, Nat. Mater. 8 (2009) 500–506.
[2] S.J. Zhang, P. Zhang, R.H. Hou, B. Li, Y.S. Zhang, K.L. Liu, X.L. Zhang, G.S. Shao, J. Energy Chem. 47 (2020) 281–290.
[3] S.J. Zhang, W.D. Xiao, Y.S. Zhang, K.L. Liu, X.D. Zhang, J.T. Zhao, Z. Wang, P. Zhang, G.S. Shao, J. Mater. Chem. A 6 (2018) 22555–22565.
[4] H.-J. Peng, J.-Q. Huang, X.-B. Cheng, Q. Zhang, Adv. Energy Mater. 7 (2017) 1770141.
[5] S.Y. Lang, R.J. Xiao, L. Gu, Y.G. Guo, R. Wen, L.J. Wan, J. Am. Chem. Soc. 140 (2018) 8147–8155.
[6] Q.L. Zou, Z.J. Liang, G.Y. Du, C.Y. Liu, E.Y. Li, Y.C. Lu, J. Am. Chem. Soc. 140 (2018) 10740–10748.
[7] S.H. Yu, X. Huang, K. Schwarz, R. Huang, T.A. Arias, J.D. Brock, H.D. Abruña, Energ. Environ. Sci. 11 (2018) 202–210.
[8] X. Liu, J.-Q. Huang, Q. Zhang, L.Q. Mai, Adv. Mater. 29 (2017) 1601759.
[9] Q.L. Li, Q.C. Zhang, C.L. Liu, Z.Y. Zhou, C.W. Li, B. He, P. Man, X.N. Wang, Y.G. Yao, J. Mater. Chem. A 7 (2019) 12997–13006.
[10] B. Han, X.L. Li, Y. Zhou, X.H. Gao, W.L. Qu, S. Zhang, C. Deng, J. Mater. Chem. A 7 (2019) 18404–18416.
[11] J.L. Yang, S.X. Zhao, X.T. Zeng, Y.M. Lu, G.Z. Cao, Adv. Mater. Interfaces 7 (2020) 1901420.
[12] Y.S. Zhang, P. Zhang, B. Li, S.J. Zhang, K.L. Liu, R.H. Hou, X.L. Zhang, S.R.P. Silva, G.S. Shao, Energy Storage Mater. 27 (2020) 159–168.
[13] X. Song, T. Gao, S.Q. Wang, Y. Bao, G.P. Chen, L.X. Ding, H.H. Wang, J. Power Sources 356 (2017) 172–180.
[14] Z. Li, B.Y. Guan, J.T. Zhang, X.W. Lou, Joule 1 (2017) 576–587.
[15] X. Yang, X. Gao, Q. Sun, S.P. Jand, Y. Yu, Y. Zhao, X. Li, K. Adair, L.Y. Kuo, J. Rohrer, J. Liang, X. Lin, M.N. Banis, Y. Hu, H. Zhang, X. Li, R. Li, H. Zhang, P. Kaghazchi, T.K. Sham, X. Sun, Adv. Mater. 31 (2019) 1901220.
[16] X.X. Li, K. Ding, B. Gao, Q.W. Li, Y.Y. Li, J.J. Fu, X.M. Zhang, P.K. Chu, K.F. Huo, Nano Energy 40 (2017) 655–662.
[17] M. Zhao, H.-J. Peng, Z.-W. Zhang, B.-Q. Li, X. Chen, J. Xie, X. Chen, J.-Y. Wei, Q. Zhang, J.-Q. Huang, Angew. Chem. Int. Ed. 58 (2019) 3779–3783.
[18] G. Zhou, L. Xu, G. Hu, L. Mai, Y. Cui, Chem. Rev. 119 (2019) 11042–11109.
[19] Z. Li, L.B. Tang, X.H. Liu, T.B. Song, Q.J. Xu, H.M. Liu, Y.G. Wang, Electrochim. Acta 310 (2019) 1–12.
[20] B. Qi, X.S. Zhao, S.G. Wang, C. Ke, L. Feng, J. Mater. Chem. A 6 (2018) 14359–14366.
[21] G. Liang, J.X. Wu, X.Y. Qin, M. Liu, Q. Li, Y.-B. He, J.-K. Kim, B.H. Li, F.Y. Kang, ACS Appl. Mater. Interfaces 8 (2016) 23105–23113.
[22] Z. Xiao, Z. Yang, L. Wang, H. Nie, M. Zhong, Q. Lai, X. Xu, L. Zhang, S. Huang, Adv. Mater. 27 (2015) 2891–2898.
[23] J.N. Wang, G.R. Yang, J. Chen, Y.P. Liu, Y.K. Wang, C.Y. Lao, K. Xi, D.W. Yang, C.J. Harris, W. Yan, S.J. Ding, R.V. Kumar, Adv. Energy Mater. 9 (2019) 1902001.
[24] G.M. Zhou, S.F. Pei, L. Li, D.-W. Wang, S.G. Wang, K. Huang, L.-C. Yin, F. Li, H.-M. Cheng, Adv. Mater. 26 (2014) 625–631.
[25] S. Tu, X. Chen, X. Zhao, M. Cheng, P. Xiong, Y. He, Q. Zhang, Y. Xu, Adv. Mater. 30 (2018) e1804581.
[26] D. Tian, X.Q. Song, M.X. Wang, X. Wu, Y. Qiu, B. Guan, X.Z. Xu, L.S. Fan, N.Q. Zhang, K.N. Sun, Adv. Energy Mater. 9 (2019) 1901940.
[27] Y. Yao, H.Y. Wang, H. Yang, S.F. Zeng, R. Xu, F.F. Liu, P.C. Shi, Y.Z. Feng, K. Wang, W.J. Yang, X.Y. Wu, W. Luo, Y. Yu, Adv. Mater. 32 (2019) 1905658.
[28] M. Zhang, W. Chen, L.X. Xue, Y. Jiao, T.Y. Lei, J.W. Chu, J.W. Huang, C.H. Gong, C.Y. Yan, Y.C. Yan, Y. Hu, X.F. Wang, J. Xiong, Adv. Energy Mater. 10 (2019) 1903008.
[29] W.G. Lim, C. Jo, A. Cho, J. Hwang, S. Kim, J.W. Han, J. Lee, Adv. Mater. 31 (2019) 1806547.
[30] Y.K. Wang, R.F. Zhang, J. Chen, H. Wu, S.Y. Lu, K. Wang, H.L. Li, C.J. Harris, K. Xi, R.V. Kumar, S.J. Ding, Adv. Energy Mater. 9 (2019) 1900953.
[31] J.-Y. Hwang, H.M. Kim, S.-K. Lee, J.-H. Lee, A. Abouimrane, M.A. Khaleel, I. Belharouak, A. Manthiram, Y.-K. Sun, Adv. Energy Mater. 6 (2016) 1501480.
[32] Z. Cui, C. Zu, W. Zhou, A. Manthiram, J.B. Goodenough, Adv. Mater. 28 (2016) 6926–6931.
[33] S.H. Gage, C. Ngo, V. Molinari, M. Causà, R.M. Richards, F.S. Gentile, S. Pylypenko, D. Esposito, J. Phys. Chem. C 122 (2018) 339–348.
[34] X.F. Wang, V. Raju, W. Luo, B. Wang, W.F. Stickle, X.L. Ji, J. Mater. Chem. A 2 (2014) 105–113.
[35] N. Jiang, H.J. Zhang, S.N. Bao, Y.G. Shen, Z.F. Zhou, Phys. B Phys. Condens. Matter 352 (2004) 118–126.
[36] Z. Li, J.T. Zhang, B.Y. Guan, X.W. Lou, Angew. Chem. Int. Ed. 56 (2017) 16003–16007.
[37] Y.K. Li, P. Zhang, D.Y. Wan, C. Xue, J.T. Zhao, G.S. Shao, Appl. Surf. Sci. 504 (2020) 144361.
[38] J. Zhao, P. Zhang, J. Fan, J. Hu, G. Shao, Appl. Surf. Sci. 430 (2018) 466–474.
[39] J. Hu, L. Wang, P. Zhang, C. Liang, G. Shao, J. Power Sources 328 (2016) 28–36.
[40] X.X. Gu, Y.Z. Wang, L. Chao, J.X. Qiu, L. Sheng, Y.L. Hou, W. Martens, N. Mahmood, S.Q. Zhang, Nano. Res. 8 (2015) 129–139.

[41] Y.H. Qu, Z.A. Zhang, X.W. Wang, Y.Q. Lai, Y.X. Liu, J. Li, J. Mater. Chem. A 1 (2013) 14306.
[42] Z. Yuan, H.J. Peng, J.-Q. Huang, X.-Y. Liu, D.-W. Wang, X.-B. Cheng, Q. Zhang, Adv. Funct. Mater. 24 (2014) 6105–6112.
[43] H.J. Sun, S.Y. Li, Y.L. Shen, F.J. Miao, P. Zhang, G.S. Shao, Appl. Surf. Sci. 47 (2020) 144001.
[44] N. Li, Y. Xie, S.T. Peng, X. Xiong, K. Han, J. Energy Chem. 42 (2020) 116–125.
[45] F.J. Miao, N. Lu, P. Zhang, Z.Y. Zhang, G.S. Shao, Adv. Func. Mater. 29 (2019) 1808994.
[46] M. Zhao, B.-Q. Li, H.-J. Peng, H. Yuan, J.-Y. Wei, J.-Q. Huang, Angew. Chem. Int. Ed. 59 (2019) 2–19.
[47] K.L. Liu, P. Zhang, F.J. Miao, S.J. Zhang, Y.S. Zhang, G.Q. Cao, G.S. Shao, J. Alloys Compd. 821 (2020) 153207.
[48] H.B. Lin, S.J. Zhang, T.R. Zhang, H.L. Ye, Q.F. Yao, G.W. Zheng, J.Y. Lee, Adv. Energy Mater. 8 (2018) 1801868.
[49] J.W. Wang, B. Zhou, H.Y. Zhao, M.M. Wu, Y.D. Yang, X.L. Sun, D.H. Wang, Y.P. Du, Mater. Chem. Front. 3 (2019) 1317–1322.
[50] F. He, J. Ye, Y. Cao, L. Xiao, H. Yang, X. Ai, ACS Appl. Mater. Interfaces 9 (2017) 11626–11633.
[51] Z.W. Seh, W. Li, J.J. Cha, G. Zheng, Y. Yang, M.T. McDowell, P.-C. Hsu, Y. Cui, Nat. Commun. 4 (2013) 1331.
[52] Z. Li, J.T. Zhang, B.Y. Guan, D. Wang, L.-M. Liu, X.W. Lou, Nat. Commun. 7 (2016) 13065.
[53] Y.F. Dong, P.F. Lu, H.D. Shi, J.Q. Qin, J. Chen, W.C. Ren, H.-M. Cheng, Z.-S. Wu, J. Energy Chem. 36 (2019) 64–73.
[54] H.-J. Peng, G. Zhang, X. Chen, Z.-W. Zhang, W.-T. Xu, J.-Q. Huang, Q. Zhang, Angew. Chem. Int. Ed. 55 (2016) 64–73.